

not a region where pathological studies show a high density of tangles in AD.²⁰ Thus, a tau imaging agent with low off-target binding in the brain remains an unmet need in the field of dementia research.⁵

PBB3 is a tau tracer developed in 2014. After preclinical evaluation, ¹¹C-PBB3 has been demonstrated to effectively visualize tau pathology in patients with AD and non-AD tauopathies.^{12,21} Notably, the high-level retention of ¹¹C-PBB3 in the AD hippocampus, wherein tau pathology is enriched, sharply contrasted with the low hippocampal retention of ¹¹C-Pittsburgh compound B (¹¹C-PIB).^{22,23} ¹¹C-PBB3 has been produced with sufficient radioactivity and high quality, demonstrating its clinical utility. Its radiosynthesis, photoisomerization, biodistribution, and metabolites have also been studied.¹² Furthermore, a previous study showed that PBB3 could bind to tau fibrils in post-mortem AD brain tissue.²¹ Recently, an ¹⁸F-labeled PBB3 derivative, ¹⁸F-APN1607 (also known as ¹⁸F-PM-PBB3), has been developed and demonstrated to improve imaging characteristics of ¹¹C-PBB3 with wider availability.²⁴ The structure of ¹⁸F-PM-PBB3 had been reported, and the results of biodistribution, metabolites, and histopathological correlation in animal and human studies had been submitted.⁵ In the present study, we applied the latest developed tracer (ie, ¹⁸F-APN1607) to evaluate the clinical and neuroimaging characteristics of tauopathies in AD patients and normal controls (NCs). We hypothesized that the ¹⁸F-APN1607 tau PET tracer could effectively display the AD-associated regions with significant tau deposition and revealed the topographical patterns of cognitive changes.

METHODS

Study Rationale

An open-label study to evaluate the performance of a novel tau imaging tracer in AD patients and NCs was conducted. Participants were recruited among patients and healthy volunteers residing in Taiwan. The study protocol was approved by the Chang Gung Memorial Hospital Institutional Review Board (CGMHIRB No. 201700982A0) and the Governmental Department of Health (1066060482). Written informed consent was obtained from all participants before the study procedure. All methods were performed in accordance with the relevant guidelines and regulations. Neurological examinations were performed on all participants. Each participant completed the following components: screening evaluation, brain MRI, ¹⁸F-AV-45 (florbetapir) PET, and ¹⁸F-APN1607 PET. The screening procedures included vital signs, ECG, physical examinations, and laboratory tests. In addition, ¹⁸F-AV-45 PET imaging results were used as part of the inclusion criteria to confirm the presence and absence of amyloid deposition in patients with probable AD and in NCs. All participants completed a series of clinical assessments and clinical safety studies to ensure that they were

medically stable after participating in this study. A final follow-up phone call for adverse event assessment was made within 7 days after ¹⁸F-APN1607 PET imaging. There were no adverse or clinically detectable pharmacologic effects in any participant. No significant changes in vital signs or the results of laboratory studies or ECG were observed either.

Subjects

A total of 22 participants comprising 12 NCs and 10 patients with probable AD were included in this study. Neuropsychological assessments, including the Mini-Mental State Examination (MMSE), the Clinical Dementia Rating (CDR) scale, and the cognitive subscale of the Alzheimer's Disease Assessment Scale (ADAS-cog) with greater scores referring to worse cognition, were administered to all participants.^{25–27} The CDR sum of box scores (CDR-SB) was used for disease severity. Participants with a diagnosis of mild to moderate probable AD (CDR, 0.5–2.0; MMSE, 10–28) ranged in age from 50 to 90 years, and were required to have positive ¹⁸F-AV-45 PET imaging results and to fulfill the NINCDS-ADRDA (National Institute for Neurological and Communicative Disorders and Stroke-Alzheimer's Disease and Related Disorder Association) criteria.²⁸ The presence of the ε2, ε3, and ε4 alleles of the apolipoprotein E (*ApoE*) gene was determined by assessing the sequences at 2 single-nucleotide polymorphisms (SNPs; rs429358 and rs7412).²⁹ Normal controls in the study were required to be 20 to 90 years old with normal cognitive function (CDR, 0; MMSE, 26–30; Wechsler Logical Memory score, >5) and negative ¹⁸F-AV-45 PET results.

Image Acquisition

¹⁸F-APN1607 was prepared and synthesized at the cyclotron facility of Chang Gung Memorial Hospital.³⁰ All participants were studied in a Biograph mCT PET/CT system (Siemens Medical Solutions, Malvern, PA) and underwent MRI to screen for other diseases (eg, hemorrhages and structural lesions) and perform spatial normalization with PET images. Brain MRI was acquired on a 3-T Siemens Magnetom TIM Trio scanner (Siemens Medical Solutions) for detailed anatomical images. High-resolution T1-weighted images were acquired with the following parameters: TR/TE, 2000/2.63 milliseconds; NEX, 1; voxel size, 1.0 × 1.0 × 1.0 mm³ (FLAIR: TR/TE, 10,000/94 milliseconds; IR, 2500 milliseconds; NEX, 2; voxel size, 0.47 × 0.47 × 5 mm³). For the ¹⁸F-APN1607 PET study, a 10-minute scan was acquired after pseudo-equilibrium in the brain was reached at 90 minute postinjection of 378 ± 11 MBq of ¹⁸F-APN1607.³¹ The PET images were then reconstructed using a 3-dimensional ordered-subset expectation maximization algorithm (4 iterations; 24 subsets; Gaussian filter, 2 mm; zoom, 3) with CT-based attenuation correction and with the scatter and random correction procedures provided by the manufacturer. The reconstructed

TABLE 1. Demographic Descriptions of Probable AD Patients and NCs

	Probable AD (n = 10)	NCs (n = 12)	P
Mean age, y	72.5 ± 10.0	56.0 ± 11.8	<0.01
Sex, male:female	4:6	7:5	0.39
Education, y	10.2 ± 3.5	14.4 ± 4.3	0.03
Onset to scan time, y	6.1 ± 2.4	—	—
Mean MMSE	12.5 ± 8.9	29.3 ± 0.9	<0.01
Mean ADAS-cog	51.3 ± 21.8	7.2 ± 4.3	<0.01
Mean CDR-SB	7.4 ± 4.6	0 ± 0	<0.01
<i>ApoE4</i> genotype (positive: negative)	4:5	2:5	0.63
Mean cortical SUVRs of ¹⁸ F-AV-45	1.41 ± 0.20	1.09 ± 0.04	<0.01
Total ICV, mL	1466.14 ± 160.61	1384.21 ± 111.72	0.19

images had a matrix size of 400 × 400 × 148 and a voxel size of 0.68 × 0.68 × 1.5 mm³. ¹⁸F-AV-45 PET scans were performed 1 month before the ¹⁸F-APN1607 PET scans. The ¹⁸F-AV-45 radiosynthesis and PET data acquisition were performed according to our previous protocols.^{32,33} Briefly, all participants underwent ¹⁸F-AV-45 PET scans on a Biograph mCT PET/CT System. PET images were acquired after IV injection of 374 ± 21 MBq of ¹⁸F-AV-45. A 10-minute scan was acquired starting at 50 minutes after the tracer injection. PET images were reconstructed using the same

method described previously, and the images were then reconstructed with a matrix size of 400 × 400 × 148 and a voxel size of 0.68 × 0.68 × 1.5 mm³.

Image Analysis

All imaging data were transformed into the Neuroimaging Informatics Technology Initiative format using the MRIcron tool (<http://www.mccauslandcenter.sc.edu/mricron/mricron/>) for further processing. For each participant, PET images (both ¹⁸F-AV-45 and

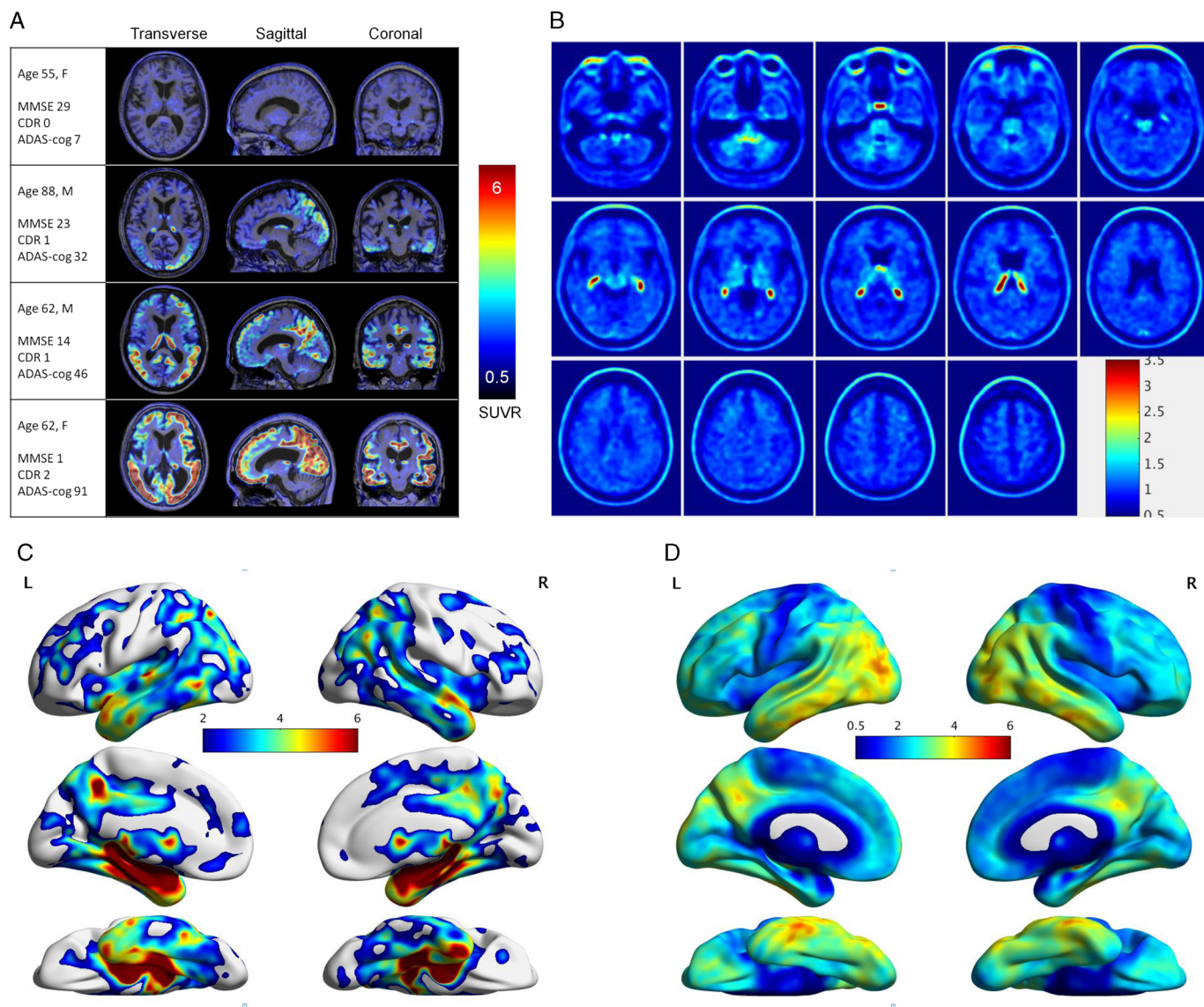


FIGURE 1. Four representative cases of ¹⁸F-APN1607 PET images overlaid with T1 MRI scans on 3 orthogonal views and the GM atrophy in patients with probable AD. **A**, A 55-year-old NC woman had MMSE score = 29, CDR = 0, and ADAS-cog score = 7. An 88-year-old man with probable AD, his MMSE score was 23, CDR = 1, and ADAS-cog score was 32. The inferior temporal and parietal regions showed increased SUVR values. The coronal view showed an increased uptake in choroid plexus region. A 62-year-old man with probable AD, his MMSE score was 14, CDR = 1, and ADAS-cog score was 46. Compared with previous case, the lateral temporal, the posterior cingulate, and the frontal regions showed increased SUVR values. A 62-year-old woman with probable AD, her MMSE score was 1, CDR = 2, and ADAS-cog score was 91. Extensively increase SUVR values in diffuse cortical regions were noted. Color map represents SUVR values. **B**, The axial view of SUVRs from averaging all ¹⁸F-APN1607 PET images in NCs. **C**, 3D surface projection view of significantly atrophic regions of GM in probable AD patients compared with NCs. Color map represents significant Z-values. **D**, 3D surface projection view of SUVRs from averaging all ¹⁸F-APN1607 PET images in patients with probable AD. Color map represents SUVR values.

¹⁸F-APN1607 images) and T1-weighted images in native space were analyzed. We coregistered each PET image to individual MRI using the SPM12 toolbox (<http://www.fil.ion.ucl.ac.uk/spm/software/spm12/>).³⁴ This procedure ensured the ¹⁸F-AV-45 PET and ¹⁸F-APN1607 images in alignment with the native MRI scans. The Muller-Gartner method was used for partial volume correction.³⁵ Then, the high-resolution MRI scans in native space were normalized to the Montreal Neurological Institute standard space with the DARTEL toolbox in SPM12.³⁶ This transform matrix was applied to PET images. The averaged intensity across the whole cerebellum was used as the reference for the ¹⁸F-AV-45 PET images, and the cerebellum gray matter (GM) considered having no amyloid, and tau pathology in AD was used as the reference region for the ¹⁸F-APN1607 PET images.³⁷ Eighteen regions of interest (ROIs), including the bilateral frontal, parietal, temporal, occipital lobes, anterior and posterior cingulate gyri, precuneus, hippocampus, and the parahippocampus, were selected based on the Harvard-Oxford cortical structural atlas, and the average values from both sides were used for further study.³⁸ Finally, the regional SUV ratios (SUVRs) from both ¹⁸F-AV-45 PET images and ¹⁸F-APN1607 PET images were calculated using the mean intensity in the target ROIs divided by the averaged intensity of the corresponding reference regions.³⁹ Analyses of GM volume was performed on T1-weighted MRI using the Computational Anatomy Toolbox, and comparisons of 2 groups were performed to search for significant atrophic regions (<http://www.neuro.uni-jena.de/cat/index.html#About>).⁴⁰ To study the regional GM atrophy in patients with AD and NCs, we first calculated the modulate GM volumes in the target ROIs and divided the individual total intracranial volume (ICV) as regional GM ratios. In NCs, the mean value from each regional GM ratio was treated as the benchmark to explore the relative atrophy in patients with AD and NCs. Finally, the regional atrophic ratio in each ROI was calculated using the following formula: regional atrophic ratio = (mean regional GM ratio – individual regional GM ratio)/mean regional GM ratio.

Statistical Analysis

All statistical analyses were performed using SPSS (version 21.0, Chicago, IL). Continuous variables were expressed as the mean ± SD. Nonparametric Mann-Whitney *U* tests and χ^2 /Fisher exact tests were performed to compare age and sex distributions between AD patients and NCs. In the MRI study, a significant level of GM atrophy between the 2 groups was defined as an uncorrected *P* value of less than 0.01 with a corresponding *t* value of greater than 2.54 and a cluster size greater than 100 voxels. For PET analysis, the effect sizes of Mann-Whitney *U* test of regional SUVrs in both ¹⁸F-AV-45 PET images and ¹⁸F-APN1607 PET images were measured by η^2 (range, 0–1) as described in the previous literature.^{41,42} Pairwise correlation using Spearman rho was used to study the associations of regional SUVrs between the ¹⁸F-AV-45 PET images and the ¹⁸F-APN1607 PET images. To study the associations between cognition and the regional SUVrs derived from the ¹⁸F-AV-45 PET images and ¹⁸F-APN1607 PET images, we performed regression analyses. To study the sequential changes of regional SUVrs in the ¹⁸F-AV-45 PET images, ¹⁸F-APN1607 PET images, and regional atrophic ratio from MRI scans, we applied a nonlinear curve fitting model using the software GraphPad Prism, version 5.0 (GraphPad Inc, San Diego, CA). Statistical significance was defined as a *P* value less than 0.01.

RESULTS

Demography

The demographic information of the 12 participants with probable AD and 10 NCs was described in Table 1. The mean age

of patients with probable AD was older than that of NCs (mean age of probable AD patients, 75.2 ± 10.0; mean age of NCs, 56.0 ± 11.8; *P* < 0.01). The mean interval from disease onset to scanning time in patients with probable AD was 6.1 ± 2.4 years. No significant group differences in sex, *ApoE4* genotype, and total ICV differences were found (*P* = 0.39, *P* = 0.63, and *P* = 0.19, respectively). Significantly lower MMSE and higher ADAD-cog and CDR-SB scores were found in patients with probable AD than in NCs (all *P*'s < 0.01). Nonparametric Mann-Whitney *U* tests revealed significantly lower GM ratios in the parietal, temporal, occipital, posterior cingulate gyrus, precuneus, hippocampus, and parahippocampus of probable AD patients than those of NCs (all *P*'s < 0.01, Supplementary Table 1, <http://links.lww.com/CNM/A273>).

Visual Description of ¹⁸F-APN1607 PET Images in Probable AD Patients and NCs

Figure 1A shows 4 representative cases of ¹⁸F-APN1607 PET images in NCs and patients with probable AD with mild or moderate stages. Upon visual inspection of ¹⁸F-APN1607 PET images in NCs, there were no prominent hyperintensities in the cortical regions (Fig. 1B). The cerebral white matter, midbrain, and basal ganglia also showed no significant uptake. In 5 of 12 NCs, the mean choroid plexus revealed approximately 2.5 to 5 times higher SUVrs than the reference regions. In patients with probable AD, the regions showing the most significantly increased uptake were the precuneus; the parietal, temporal, and frontal regions; and the parahippocampal region. The medial occipital region and the insular cortex showed weakly increased tracer uptake compared with the reference regions. The choroid plexus showed increased tracer uptake in 7 of 10 patients with probable AD. As for GM, patients with probable AD showed significant GM atrophy in the bilateral medial temporal, precuneus, and parietal regions, a topographical distribution similar to that of tau deposition from averaging ¹⁸F-APN1607 PET images of all patients with probable AD (Figs. 1C–D).

Regional Differences of SUVrs in ¹⁸F-APN1607 and ¹⁸F-AV-45 PET Images

Nonparametric Mann-Whitney *U* tests were performed to study the regional differences in ¹⁸F-APN1607 PET images between patients with probable AD and NCs. Table 2 shows that the frontal, parietal, temporal, and occipital lobes; the anterior and posterior cingulate gyri; the precuneus; and the parahippocampal region had significantly higher SUVrs in probable AD patients than in NCs (all *P*'s < 0.01). The effect sizes in all of the above regions were medium to large (η^2 = 0.44–0.75). The hippocampal region did not show a significant group difference (*P* = 0.14). In the ¹⁸F-AV-45 PET imaging study, patients with AD showed significantly higher SUVrs in the frontal, parietal, temporal, and occipital lobes; the anterior and posterior cingulate gyri; and the precuneus region (all *P*'s < 0.01). There were no significant group differences in the hippocampal and parahippocampal regions (*P* = 0.08 and 0.81, respectively). The effect size values from ¹⁸F-AV-45 PET images were smaller than those from ¹⁸F-APN1607 PET images in most regions. Table 3 shows the results of pairwise correlations of regional SUVrs derived from the ¹⁸F-AV-45 PET images and the ¹⁸F-APN1607 PET images. The values of Spearman rho (rank-correlation coefficient) showed significant associations in the frontal, temporal, parietal, and occipital lobes; the anterior and posterior cingulate gyri; and the precuneus region. Interestingly, the SUVrs of the parahippocampus from the ¹⁸F-APN1607 PET images had significant associations with those of all the above regions (all *P*'s < 0.01), but the values from the ¹⁸F-AV-45 PET images did not. The SUVrs from the hippocampal region showed no significant associations with any of the regions. These results demonstrated similar trends of the tau and amyloid

TABLE 2. Comparison of Regional SUVRs From ¹⁸F-APN1607 and ¹⁸F-AV-45 PET Imaging Between Probable AD Patients and NCs

Regions	Mean Cortical SUVRs of ¹⁸ F-APN1607 (Mean ± SD)				Mean Cortical SUVRs of ¹⁸ F-AV-45 (Mean ± SD)			
	Probable AD	NCs	P	Effect Size (η ²)	Probable AD	NCs	P	Effect Size (η ²)
Frontal	1.89 ± 0.93	0.86 ± 0.12	<0.01	0.69	1.64 ± 0.35	1.01 ± 0.14	<0.01	0.58
Parietal	2.47 ± 1.22	0.94 ± 0.11	<0.01	0.75	1.63 ± 0.32	1.02 ± 0.11	<0.01	0.65
Temporal	2.46 ± 0.95	0.99 ± 0.10	<0.01	0.75	1.64 ± 0.34	1.06 ± 0.09	<0.01	0.65
Occipital	2.43 ± 1.17	0.97 ± 0.11	<0.01	0.75	1.59 ± 0.31	0.97 ± 0.13	<0.01	0.71
Anterior cingulate gyrus	1.62 ± 0.69	0.94 ± 0.12	<0.01	0.44	1.76 ± 0.35	1.17 ± 0.19	<0.01	0.58
Posterior cingulate gyrus	2.63 ± 1.09	1.02 ± 0.09	<0.01	0.75	1.95 ± 0.37	1.13 ± 0.15	<0.01	0.63
Precuneus	2.67 ± 1.44	0.98 ± 0.09	<0.01	0.75	1.86 ± 0.38	1.05 ± 0.11	<0.01	0.68
Hippocampus	1.90 ± 0.74	1.47 ± 0.76	0.141	0.10	0.95 ± 0.16	1.06 ± 0.99	0.08	0.15
Parahippocampus	2.06 ± 0.69	0.97 ± 0.11	<0.01	0.52	0.93 ± 0.20	0.96 ± 0.07	0.81	0.01

depositions between the parahippocampus and the rest of the studied brain regions, but the hippocampus failed to show the same pattern.

Correlation Studies Between Regional SUVRs and Clinical Parameters

To explore the correlations between regional SUVRs and clinical scores in ¹⁸F-APN1607 PET images, we performed regression analyses in patients with probable AD and in NCs. The SUVRs of the frontal, parietal, temporal, and occipital lobes; the anterior and posterior cingulate gyri; the precuneus; and the parahippocampal regions showed significant correlations with the ADAS-cog scores (all P's < 0.01). The values of R² ranged from 0.54 to 0.68. The hippocampus did not show a significant association with the ADAS-cog scores (P = 0.53). Figure 2 shows the significant correlation between the regional SUVRs of the posterior cingulate gyrus and the ADAS-cog scores. Age, sex, and ApoE4 gene were used as covariates in the regression model, and there were no significant associations with regional SUVRs (P = 0.23, P = 0.67, and P = 0.85, respectively). The CDR-SB showed significant associations with the above regions, and the values of R² ranged from 0.52 to 0.61 (all P's < 0.01), except for the hippocampus regions (P = 0.77). In ¹⁸F-AV-45 PET images, regional SUVRs of the frontal, parietal, temporal, and occipital lobes; the anterior and posterior cingulate gyri; and the precuneus region showed significant associations with the ADAS-cog scores (all P's < 0.01). The regional SUVRs from the parietal, temporal, and occipital lobes; the posterior cingulate gyrus; and the precuneus region showed significant associations with CDR-SB (all P's < 0.01).

Relations Between Regional SUVRs in ¹⁸F-APN1607 and ¹⁸F-AV-45 PET Images and Cognitive Status

To further explore the relationship between regional SUVRs in ¹⁸F-APN1607 PET images and the ADAS-cog scores, we used the sigmoidal 4-parameter logistic curve fitting model (Fig. 3A). The SUVRs in the parahippocampal region rapidly increased values as the ADAS-cog scores increased and then reached a plateau. This was followed by increased SUVRs of the posterior cingulate gyrus and the temporal, frontal, parietal, and occipital regions, whose values sequentially increased as the ADAS-cog scores increased (Fig. 3B). Quantitative analysis indicated that the ADAS-cog scores at the inflection points of the sigmoidal curves from the above regions showed the lowest value in the parahippocampus (20.3), followed by the precuneus (38.6), temporal lobe (39.9), posterior cingulate gyrus (42.5), frontal lobe (42.5), parietal lobe (45.7), anterior cingulate gyrus (51.5), and occipital lobe (56). Figure 4 shows the combination of SUVRs from the ¹⁸F-AV-45 and ¹⁸F-APN1607 PET images and regional atrophic ratios in the different ROIs. In most regions, the SUVRs from the ¹⁸F-AV-45 PET images rapidly increased as the ADAS-cog scores increased, except the parahippocampus region (Fig. 4A), which did not show increased uptake as the ADAS-cog scores increased. The SUVRs in most ROIs from the ¹⁸F-APN1607 PET images showed gradual increases and reached plateaus as the ADAS-cog scores increased, except the occipital region. The regional atrophic ratios from T1-weighted MRI showed flatter curves of increase, compared with the curves from the ¹⁸F-APN1607 PET images as the ADAS-cog scores increased, except the parahippocampus region.

TABLE 3. Pairwise Correlation of Regional SUVRs Between ¹⁸F-AV-45 PET Imaging (Rows) and ¹⁸F-APN1607 PET Imaging (Columns)

Regions					Anterior	Posterior			
	Frontal	Parietal	Temporal	Occipital	Cingulate Gyrus	Cingulate Gyrus	Precuneus	Hippocampus	Parahippocampus
Frontal	0.82**	0.75**	0.73**	0.77**	0.75**	0.73**	0.77**	-0.26	0.17
Parietal	0.79**	0.74**	0.69**	0.75**	0.71**	0.70**	0.76**	-0.39	0.08
Temporal	0.73**	0.67**	0.65**	0.70**	0.64**	0.64**	0.69**	-0.29	0.05
Occipital	0.78**	0.75**	0.67*	0.77**	0.72**	0.70**	0.73**	-0.39	0.10
Anterior cingulate gyrus	0.64**	0.59**	0.49	0.63**	0.65**	0.56**	0.61**	-0.15	0.16
Posterior cingulate gyrus	0.86**	0.83**	0.75**	0.86**	0.81**	0.83**	0.88**	-0.41	0.21
Precuneus	0.86**	0.82**	0.75**	0.86**	0.78**	0.79**	0.85**	-0.41	0.19
Hippocampus	0.41	0.48	0.47	0.41	0.44	0.37	0.44	0.11	0.28
Parahippocampus	0.65**	0.58**	0.56**	0.61**	0.61**	0.53	0.63**	-0.19	0.14

Spearman rho (rank correlation coefficient) values. *P < 0.01.

DISCUSSION

In the current work, we applied the most recently developed tau tracer, ^{18}F -APN1607, in a group of patients with probable AD and a group of NCs. Our study showed several advantages of this new tau tracer. First, this tracer revealed a clear background in the midbrain, basal ganglia, and cerebral white matter regions in NCs. In patients with probable AD, the tracer demonstrated significantly increasing intensities in AD-associated cortical regions with medium to large effect sizes (mean effect size = 0.71 in the significant regions). Second, the regional SUVRs in AD-associated cortical regions showed significant correlations with the ADAS-cog scores and CDR-SB, suggesting that tau deposition correlated with clinical severity in vivo. Third, the pattern of sequentially increasing regional SUVRs from the ^{18}F -APN1607 PET images corresponding well with disease severity and hence revealed the topographical progression of tau distribution in AD. Finally, the combined ^{18}F -AV-45, ^{18}F -APN1607 PET, and regional atrophic ratio information from the same region could support the hypothesis that amyloid deposition would reach a plateau earlier than tau deposition before neuronal degeneration revealed.⁴³ These results are in line with the pathological observations from the progression of AD.²⁰

The Characteristics of In Vivo ^{18}F -APN1607 PET Imaging

In vivo imaging of the deposition of tau proteins faced several inherent obstacles, such as the intracellular deposition of tau aggregates, the 6 different isoforms of tau, the similarity of the β -sheet structure between tau and many other misfolded proteins, and the colocalization of tau with 5 to 20 times its concentration in β -amyloid protein in GM areas.⁴⁴ Despite these challenges, several tau tracers have been synthesized in the past few years. The first-generation tracers (eg, ^{18}F -THK-5317, ^{18}F -THK-5351, ^{18}F -AV-1451, and ^{11}C -PBB3) have been extensively used in research studies. The second-generation compounds, namely, ^{18}F -MK-6240, ^{18}F -JNJ-64349311, ^{18}F -PI-2620, ^{18}F -GTP1, and ^{18}F -APN1607, have started to be used for in vivo studies.^{14,45} The advantages of the second-generation compounds include a lack of off-target binding in the basal ganglia and thalamus and a relatively low affinity for

the enzyme MAO-B.^{46–48} A directly head-to-head comparison between the first-generation and second-generation tau tracers also revealed that different molecular binding targets existed in these tracers.⁴⁹ In the current study, we showed that there is no significant uptake of the PET tracer ^{18}F -APN1607 in the midbrain or the basal ganglia. Similar study results have been found using ^{11}C -PBB3 in healthy participants and using autoradiographic methods in human tissue.^{50,51} These tracers could be beneficial for research on various tau-related neurodegenerative diseases, such as progressive supranuclear palsy and corticobasal syndrome. Furthermore, the AD-associated cortical regions of subjects with probable AD showed significantly increased SUVRs in ^{18}F -APN1607 PET images, with medium to large effect size, which could be used to easily distinguish the abnormal cortical regions in clinical practice. In the current work, the tracer ^{18}F -APN1607 still had off-target binding in the choroid plexus in 5 (42%) of 12 NCs and in 7 (70%) of 10 participants with probable AD. From a previous autoradiographic study using ^{18}F -THK-5351 or ^{18}F -AV-1451 in postmortem human brains, these first-generation tau tracers had strong binding properties in tissue with a high density of melanin-containing cells.⁵¹ The compound ^{18}F -APN1607 may have similar characteristics. There are also other possible explanations that have been mentioned; for example, the epithelial cells of the choroid plexus contain tangle-like structures that could be labeled by ^{18}F -AV-1451, or the choroid plexus could act as a gatekeeper for the accumulation of tau protein.^{52,53}

Significant Associations Between Regional SUVRs in ^{18}F -APN1607 PET and Clinical Scores

In previous AD studies, cognitive decline and tau accumulation showed a close relationship.^{54–56} Based on investigations using ^{18}F -AV-1451, Aschenbrenner et al⁵⁷ suggested that increasing levels of tau most consistently relate to declines in cognition in patients with AD. In our results, SUVRs in ^{18}F -APN1607 PET images from AD-associated regions showed significantly positive correlations with the ADAS-cog scores and CDR-SB scores ($P < 0.01$), which demonstrated that increasing tau burden correlated with decreasing cognition and increasing disease severity. The SUVRs in AD-associated regions shown on ^{18}F -AV-45 PET images also showed significant associations with the ADAS-cog scores and CDR-SB scores, which may be related to the small sample size in this study.

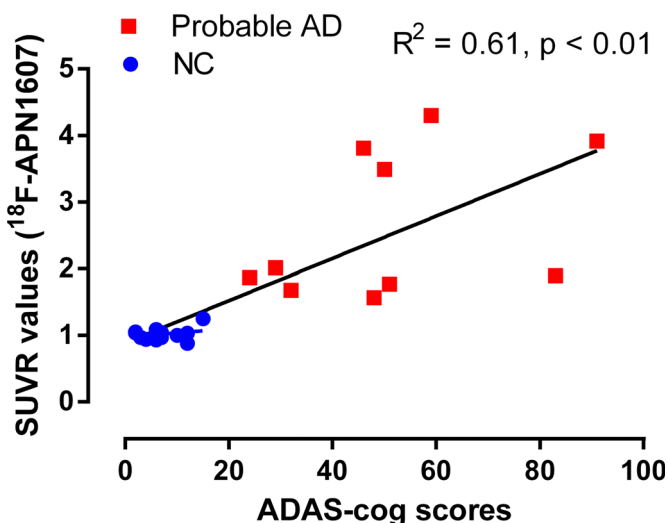


FIGURE 2. Significant correlation between the ADAS-cog scores and regional SUVRs determined from ^{18}F -APN1607 PET images of the posterior cingulate gyrus.

The Sequential Changes in Regional SUVRs From ^{18}F -APN1607 PET Imaging

The pathological study showed that the spread of tau deposits started from the entorhinal cortex (Braak stages I/II), moving to the inferolateral temporal cortex and parts of the medial parietal lobe (stages III/IV), and eventually spreading throughout the association cortex (V/VI).^{20,58} Our results using in vivo ^{18}F -APN1607 PET images demonstrated a similar topographical pattern. At least 3 patterns of tau deposition could be found (Fig. 3A). The first pattern was in the parahippocampal region; tau deposition rapidly increased and then reached a plateau (rapid saturation) as the ADAS-cog scores increased. The second pattern was in the posterior cingulate gyrus and the temporal, frontal, and parietal regions, undergoing a slow progressive increase in tau deposits and then reaching to plateaus. The final pattern was in the occipital region, which showed a gradual increase of tau deposition without a plateau (Fig. 3). The ADAS-cog scores at the inflection points of the sigmoidal curves showed the lowest value in the parahippocampus, followed by the precuneus, temporal lobe, posterior cingulate gyrus, frontal lobe, parietal lobe, anterior cingulate gyrus, and occipital lobe. These findings were in agreement with the previous neuropathological

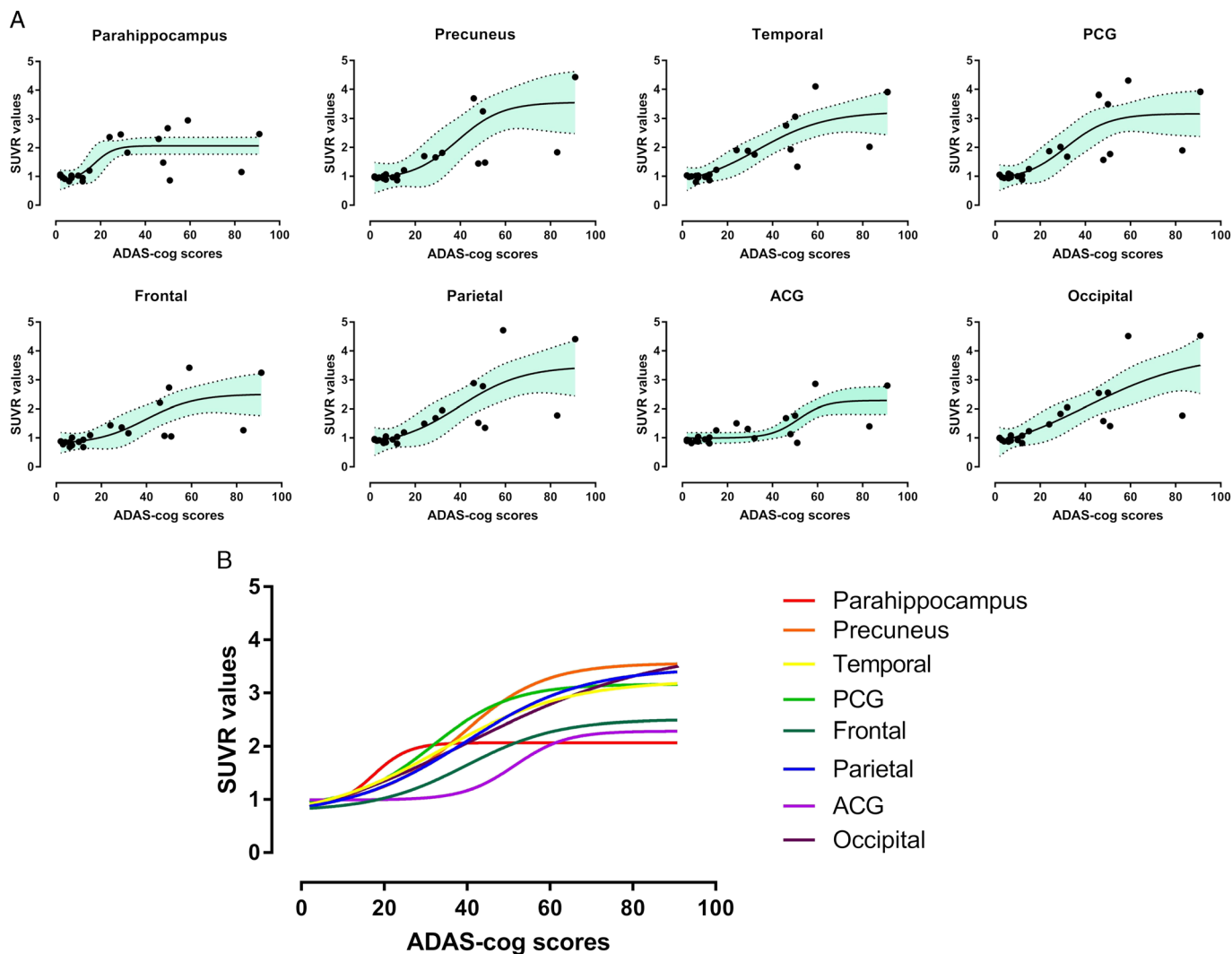


FIGURE 3. Sequentially increased regional SUVRs in ¹⁸F-APN1607 PET images from patients with probable AD. **A**, Logistic curve fitting method was applied to the SUVRs of the parahippocampus, precuneus, temporal, posterior cingulate gyrus, frontal, parietal, the anterior cingulate gyrus, and the occipital regions as the ADAS-cog scores increased. The blue area showed the 95% confidence interval area. The solid lines showed the mean fitting curves. **B**, Combined fitting curves from all above regions showed the parahippocampal region had rapid saturation as the ADAS-cog scores increased, whereas the cingulate gyrus and the temporal, frontal, and parietal regions showed sigmoidally increasing uptake. The occipital region showed gradually increasing uptake without a plateau.

evidence of neurofibrillary changes from transentorhinal stages to limbic stages and finally to neocortical stages.²⁰

The Evolution of Amyloid, Tau, and Atrophic Changes in Different Regions

In most of the ROIs, the evolution of SUVRs from ¹⁸F-AV-45 and ¹⁸F-APN1607 PET images and regional atrophic ratios showed that the amyloid burden usually rapidly increased to a plateau as the ADAS-cog scores increased, especially in the low ranges of ADAS-cog scores. The patterns of increasing tau deposition were regionally dependent. Finally, the regional atrophic ratios from MRI showed progressively increased values without plateaus (Fig. 4).

When we combined the SUVRs from ¹⁸F-AV-45 and ¹⁸F-APN1607 PET images and regional atrophic ratio information in the same ROIs to explore the sequential changes, we found that

the amyloid burden usually manifested earlier than tau deposition, and tau deposition usually started earlier than regional atrophies in most regions (Fig. 4). In the parahippocampal region, tau deposition and regional atrophic ratio rapidly increased in the low ADAS-cog scores range, but the amyloid burden did not show a significant increase (Fig. 4A). On the other hand, the occipital region showed a progressive increase of tau deposition and regional atrophy without a plateau phase (Fig. 4B). These findings may indicate that cerebral amyloid deposition reached a saturation state more rapidly than tau deposition and neurodegeneration in most areas, but this sequential change also had the regional variability. Currently, our findings from the cross-sectional data could demonstrate the importance of amyloid-tau-neurodegeneration sequential changes in regional base level, which were compatible with the widely hypothesized model of AD and amyloid-tau-neurodegeneration classification system in the AD research framework.^{59,60}

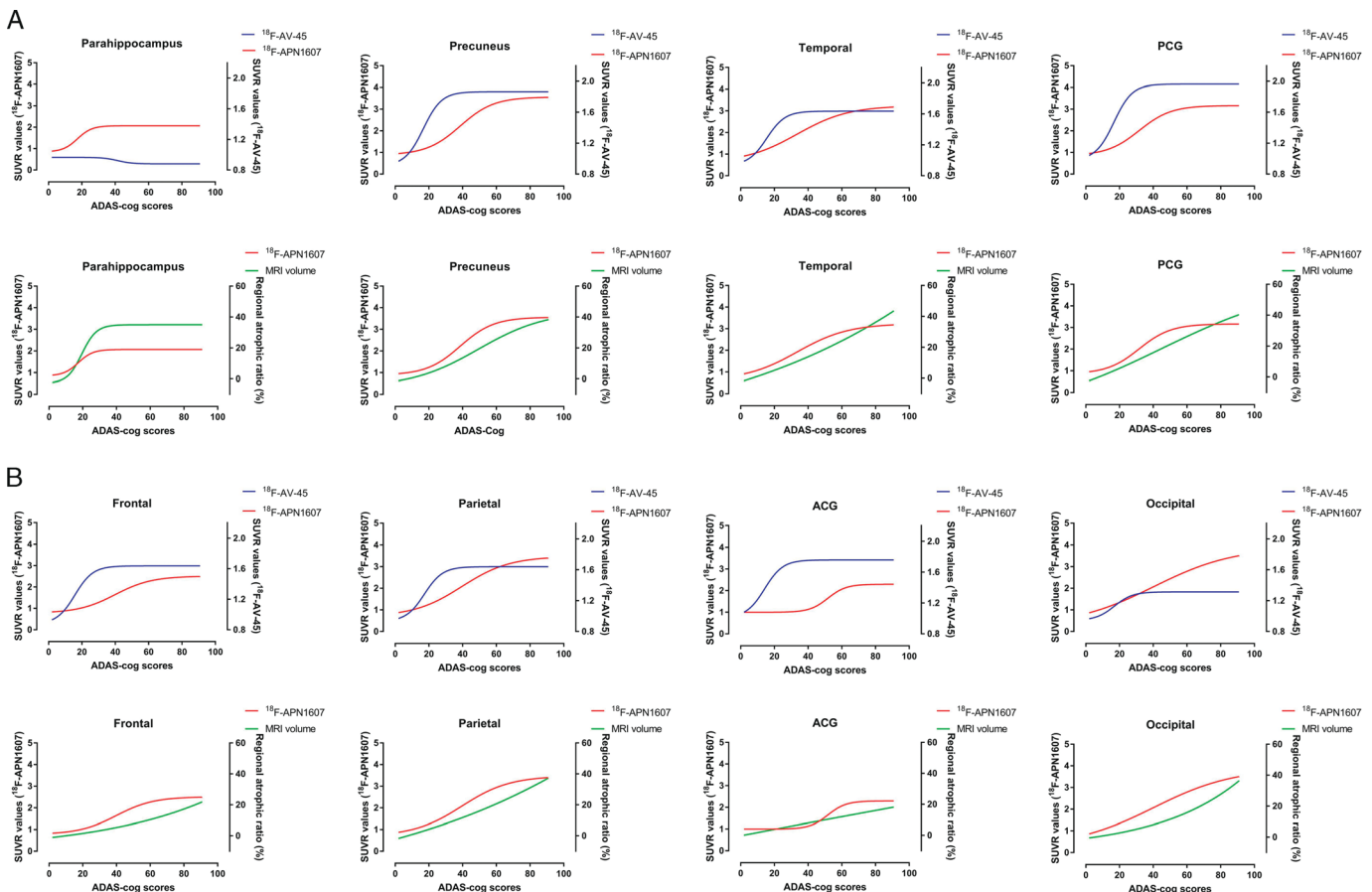


FIGURE 4. The evolution of increased SUVRs from ^{18}F -AV-45 PET, ^{18}F -APN1607 PET imaging, and regional atrophic ratios in (A) the parahippocampus, the precuneus, the temporal, and the posterior cingulated gyrus regions, and (B) the frontal, the parietal, the anterior cingulate gyrus, and the occipital regions. The SUVRs of ^{18}F -AV-45 PET and ^{18}F -APN1607 PET and regional atrophic ratios were fit for the ADAS-cog scores. In most regions, the amyloid burden showed rapid saturation as the ADAS-cog scores increased, whereas uptake associated with tau depositions were slowly increased. Finally, the regional atrophic ratios were gradually increased. ACG, anterior cingulated gyrus; PCG, posterior cingulated gyrus.

Limitations

Several limitations of the current work need to be addressed. First, the tau tracer ^{18}F -APN1607 is a relatively new tracer, thus the pathological results are not yet available in our study. Up to now, only postmortem brain tissue had been studied with this tracer, and there have been no clinicopathological correlation studies using this tracer yet.²¹ Furthermore, the 6 isoforms of tau in the brain include 3R and 4R tau, whose misfolding is responsible for various neurodegenerative diseases, such as progressive supranuclear palsy, corticobasal syndrome, and frontotemporal dementia.⁶¹ Whether the tau tracer ^{18}F -APN1607 can differentiate among all isoforms is an open question that needs further investigation. In addition, direct application of MAO-B inhibitors in patients undergoing ^{18}F -APN1607 PET imaging has not been performed, and it could be difficult to eliminate these concerns about the first-generation tau tracers.¹⁵ Second, our study had a small sample size, a significant age difference between AD patients and NCs, and no participants with amnesic mild cognitive impairment. We acknowledge the demographic differences between groups, and we used age and sex as covariates to study the correlations of regional SUVRs from ^{18}F -APN1607 PET imaging with ADAS-cog and CDR-SB scores. Increasing the sample size and adding amnesic patients will help us explore the

features of this tau tracer. Third, we used the ADAS-cog scores as the severity index for curve fitting with the regional SUVRs from ^{18}F -AV-45, ^{18}F -APN1607 PET images, and regional atrophy ratios. We acknowledge that any biomarker changes to be incorporated into the hypothetical model of AD should come from longitudinal studies rather than cross-sectional observations, and our findings must be interpreted conservatively. Future studies should focus on longitudinal changes in ^{18}F -APN1607 PET imaging with the aid of other biomarkers, which may provide further evidence for the AD hypothetical model.

CONCLUSIONS

This is the first in vivo study of the PET tracer ^{18}F -APN1607 in patients with mild to moderate AD. Our findings suggest that ^{18}F -APN1607 PET imaging has a clear background and no off-target binding in the basal ganglia or the thalamus. The regional SUVRs of the AD-associated regions were significantly correlated with cognitive deficits and disease severity. Finally, combined tau imaging with information on amyloid deposition and neurodegeneration may further our understanding of dynamic biomarker changes in the regional base level during the progression of AD.

ACKNOWLEDGMENTS

The authors thank the patients and healthy individuals for their participation in this study. This study was carried out with support from the grants of the Research Fund of Chang Gung Memorial Hospital (CMRPG3J0351 and CMRPG3J0371).

REFERENCES

- Lee VM, Goedert M, Trojanowski JQ. Neurodegenerative tauopathies. *Annu Rev Neurosci*. 2001;24:1121–1159.
- McKee AC, Cantu RC, Nowinski CJ, et al. Chronic traumatic encephalopathy in athletes: progressive tauopathy after repetitive head injury. *J Neuropathol Exp Neurol*. 2009;68:709–735.
- Villemagne VL, Okamura N. Tau imaging in the study of ageing, Alzheimer's disease, and other neurodegenerative conditions. *Curr Opin Neurobiol*. 2016;36:43–51.
- Okamura N, Harada R, Ishiki A, et al. The development and validation of tau PET tracers: current status and future directions. *Clin Transl Imaging*. 2018;6:305–316.
- Leuzy A, Chiotis K, Lemoine L, et al. Tau PET imaging in neurodegenerative tauopathies—still a challenge. *Mol Psychiatry*. 2019;24:1112–1134.
- Xia CF, Arteaga J, Chen G, et al. [(18)F]T807, a novel tau positron emission tomography imaging agent for Alzheimer's disease. *Alzheimers Dement*. 2013;9:666–676.
- Chien DT, Bahri S, Szardenings AK, et al. Early clinical PET imaging results with the novel PHF-tau radioligand [F-18]-T807. *J Alzheimers Dis*. 2013;34:457–468.
- Harada R, Okamura N, Furumoto S, et al. [(18)F]THK-5117 PET for assessing neurofibrillary pathology in Alzheimer's disease. *Eur J Nucl Med Mol Imaging*. 2015;42:1052–1061.
- Stepanov V, Svedberg M, Jia Z, et al. Development of [¹¹C]/[³H]THK-5351 - a potential novel carbon-11 tau imaging PET radioligand. *Nucl Med Biol*. 2017;46:50–53.
- Hsiao IT, Lin KJ, Huang KL, et al. Biodistribution and radiation dosimetry for the tau tracer ¹⁸F-THK-5351 in healthy human subjects. *J Nucl Med*. 2017;58:1498–1503.
- Bethausen TJ, Ellison PA, Murali D, et al. Characterization of the radiosynthesis and purification of [¹⁸F]THK-5351, a PET ligand for neurofibrillary tau. *Appl Radiat Isot*. 2017;130:230–237.
- Hashimoto H, Kawamura K, Igarashi N, et al. Radiosynthesis, photoisomerization, biodistribution, and metabolite analysis of ¹¹C-PBB3 as a clinically useful PET probe for imaging of tau pathology. *J Nucl Med*. 2014;55:1532–1538.
- Walji AM, Hostetler ED, Selnick H, et al. Discovery of 6-(Fluoro-(18)F)-3-(1H-pyrrolo[2,3-c]pyridin-1-yl)isoquinolin-5-amine ([¹⁸F]-MK-6240): a positron emission tomography (PET) imaging agent for quantification of neurofibrillary tangles (NFTs). *J Med Chem*. 2016;59:4778–4789.
- Declercq L, Rombouts F, Koole M, et al. Preclinical evaluation of (18)F-JNJ64349311, a novel PET tracer for tau imaging. *J Nucl Med*. 2017;58:975–981.
- Ng KP, Pascoal TA, Mathotaarachchi S, et al. Monoamine oxidase B inhibitor, selegiline, reduces ¹⁸F-THK5351 uptake in the human brain. *Alzheimers Res Ther*. 2017;9:25.
- Marque M, Normandin MD, Vanderburg CR, et al. Validating novel tau positron emission tomography tracer [F-18]-AV-1451 (T807) on postmortem brain tissue. *Ann Neurol*. 2015;78:787–800.
- Hostetler ED, Walji AM, Zeng Z, et al. Preclinical characterization of ¹⁸F-MK-6240, a promising PET tracer for in vivo quantification of human neurofibrillary tangles. *J Nucl Med*. 2016;57:1599–1606.
- Huang KL, Hsu JL, Lin KJ, et al. Visualization of ischemic stroke-related changes on ¹⁸F-THK-5351 positron emission tomography. *EJNMMI Res*. 2018;8:62.
- Lee H, Seo S, Lee SY, et al. [¹⁸F]-THK5351 PET imaging in patients with semantic variant primary progressive aphasia. *Alzheimer Dis Assoc Disord*. 2018;32:62–69.
- Braak H, Braak E. Neuropathological staging of Alzheimer-related changes. *Acta Neuropathol*. 1991;82:239–259.
- Ono M, Sahara N, Kumata K, et al. Distinct binding of PET ligands PBB3 and AV-1451 to tau fibril strains in neurodegenerative tauopathies. *Brain*. 2017;140:764–780.
- Maruyama M, Shimada H, Suhara T, et al. Imaging of tau pathology in a tauopathy mouse model and in Alzheimer patients compared to normal controls. *Neuron*. 2013;79:1094–1108.
- Wood H. Alzheimer disease: [¹¹C]PBB3—a new PET ligand that identifies tau pathology in the brains of patients with AD. *Nat Rev Neurol*. 2013;9:599.
- Shimada H, Ono M, Tagai K, et al. Preclinical and clinical characterization of ¹⁸F-PM-PBB3, a PET ligand for diverse tau pathologies. *Alzheimers Dement*. 2018;14:P318–P319.
- Doraiswamy PM, Krishen A, Stallone F, et al. Cognitive performance on the Alzheimer's Disease Assessment Scale: effect of education. *Neurology*. 1995;45:1980–1984.
- Folstein MF, Folstein SE, McHugh PR. "Mini-Mental State". A practical method for grading the cognitive state of patients for the clinician. *J Psychiatr Res*. 1975;12:189–198.
- Hughes CP, Berg L, Danziger WL, et al. A new clinical scale for the staging of dementia. *Br J Psychiatry*. 1982;140:566–572.
- McKhann G, Drachman D, Folstein M, et al. Clinical diagnosis of Alzheimer's disease: report of the NINCDS-ADRDA work group under the auspices of Department of Health and Human Services Task Force on Alzheimer's disease. *Neurology*. 1984;34:939–944.
- Liao YC, Lee WJ, Hwang JP, et al. ABCA7 gene and the risk of Alzheimer's disease in Han Chinese in Taiwan. *Neurobiol Aging*. 2014;35:2423.e7–2423.e13.
- Weng CC, Hsiao IT, Yang QF, et al. Characterization of ¹⁸F-PM-PBB3 (¹⁸F-APN-1607) uptake in the rTg510 mouse model of tauopathy. *Molecules*. 2020;25:1750.
- Huang CC, Hsiao IT, Lin KJ, et al. Optimal scanning time for the novel tau PET tracer ¹⁸F-APN-1607. *13th Human Amyloid Imaging*. 2019;P392.
- Lin KJ, Hsu WC, Hsiao IT, et al. Whole-body biodistribution and brain PET imaging with [¹⁸F]AV-45, a novel amyloid imaging agent—a pilot study. *Nucl Med Biol*. 2010;37:497–508.
- Hsiao IT, Huang CC, Hsieh CJ, et al. Perfusion-like template and standardized normalization-based brain image analysis using ¹⁸F-florbetapir (AV-45/Amyvid) PET. *Eur J Nucl Med Mol Imaging*. 2013;40:908–920.
- Ashburner J, Friston KJ. Unified segmentation. *Neuroimage*. 2005;26:839–851.
- Gonzalez-Escamilla G, Lange C, Teipel S, et al. PETPVE12: an SPM toolbox for partial volume effects correction in brain PET - application to amyloid imaging with AV45-PET. *Neuroimage*. 2017;147:669–677.
- Ashburner J. A fast diffeomorphic image registration algorithm. *Neuroimage*. 2007;38:95–113.
- Scholl M, Lockhart SN, Schonhaut DR, et al. PET imaging of tau deposition in the aging human brain. *Neuron*. 2016;89:971–982.
- Frazier JA, Chiu S, Breeze JL, et al. Structural brain magnetic resonance imaging of limbic and thalamic volumes in pediatric bipolar disorder. *Am J Psychiatry*. 2005;162:1256–1265.
- Joshi AD, Pontecorvo MJ, Clark CM, et al. Performance characteristics of amyloid PET with florbetapir F 18 in patients with Alzheimer's disease and cognitively normal subjects. *J Nucl Med*. 2012;53:378–384.
- Gaser C, Nenadic I, Buchsbaum BR, et al. Deformation-based morphometry and its relation to conventional volumetry of brain lateral ventricles in MRI. *Neuroimage*. 2001;13:1140–1145.
- Sawilowsky SS. New effect size rules of thumb. *J Mod Appl Stat Methods*. 2009;8:597–599.
- Fritz CO, Morris PE, Richler JJ. Effect size estimates: current use, calculations, and interpretation. *J Exp Psychol Gen*. 2012;141:2–18.
- Mouhi A, Duchesne S. Alzheimer's disease neuroimaging I. Toward a dynamic biomarker model in Alzheimer's disease. *J Alzheimers Dis*. 2012;30:91–100.
- Villemagne VL, Okamura N. In vivo tau imaging: obstacles and progress. *Alzheimers Dement*. 2014;10:S254–S264.
- Pascoal TA, Shin M, Kang MS, et al. In vivo quantification of neurofibrillary tangles with [¹⁸F]MK-6240. *Alzheimers Res Ther*. 2018;10:74.
- Aguero C, Dhaynaut M, Normandin MD, et al. Autoradiography validation of novel tau PET tracer [F-18]-MK-6240 on human postmortem brain tissue. *Acta Neuropathol Commun*. 2019;7:37.
- Murugan NA, Chiotis K, Rodriguez-Vieitez E, et al. Cross-interaction of tau PET tracers with monoamine oxidase B: evidence from in silico modelling and in vivo imaging. *Eur J Nucl Med Mol Imaging*. 2019;46:1369–1382.
- Villemagne V, Dore V, Mulligan R, et al. Evaluation of ¹⁸F-PI-2620, a second-generation selective tau tracer for the assessment of Alzheimer's and non-Alzheimer's tauopathies. *J Nucl Med*. 2018;59:410.
- Chiotis K, Stenkrona P, Almkvist O, et al. Dual tracer tau PET imaging reveals different molecular targets for ¹¹C-THK5351 and ¹¹C-PBB3 in the Alzheimer brain. *Eur J Nucl Med Mol Imaging*. 2018;45:1605–1617.

50. Perez-Soriano A, Arena JE, Dinelle K, et al. PBB3 imaging in Parkinsonian disorders: evidence for binding to tau and other proteins. *Mov Disord*. 2017; 32:1016–1024.
51. Tago T, Toyohara J, Harada R, et al. Characterization of the binding of tau imaging ligands to melanin-containing cells: putative off-target-binding site. *Ann Nucl Med*. 2019;33:375–382.
52. Ikonovic MD, Abrahamson EE, Price JC, et al. [F-18]AV-1451 positron emission tomography retention in choroid plexus: more than “off-target” binding. *Ann Neurol*. 2016;80:307–308.
53. Raha-Chowdhury R, Henderson JW, Raha AA, et al. Choroid plexus acts as gatekeeper for TREM2, abnormal accumulation of ApoE, and fibrillary tau in Alzheimer’s disease and in Down syndrome dementia. *J Alzheimers Dis*. 2019;69:91–109.
54. Ossenkoppele R, Schonhaut DR, Scholl M, et al. Tau PET patterns mirror clinical and neuroanatomical variability in Alzheimer’s disease. *Brain*. 2016;139:1551–1567.
55. Johnson KA, Schultz A, Betensky RA, et al. Tau positron emission tomographic imaging in aging and early Alzheimer disease. *Ann Neurol*. 2016; 79:110–119.
56. Ossenkoppele R, Smith R, Ohlsson T, et al. Associations between tau, A β , and cortical thickness with cognition in Alzheimer disease. *Neurology*. 2019;92:e601–e612.
57. Aschenbrenner AJ, Gordon BA, Benzinger TLS, et al. Influence of tau PET, amyloid PET, and hippocampal volume on cognition in Alzheimer disease. *Neurology*. 2018;91:e859–e866.
58. Lowe VJ, Wiste HJ, Senjem ML, et al. Widespread brain tau and its association with ageing, Braak stage and Alzheimer’s dementia. *Brain*. 2018; 141:271–287.
59. Jack CR Jr, Knopman DS, Jagust WJ, et al. Tracking pathophysiological processes in Alzheimer’s disease: an updated hypothetical model of dynamic biomarkers. *Lancet Neurol*. 2013;12:207–216.
60. Jack CR Jr, Bennett DA, Blennow K, et al. NIA-AA research framework: toward a biological definition of Alzheimer’s disease. *Alzheimers Dement*. 2018;14:535–562.
61. Choi Y, Ha S, Lee YS, et al. Development of tau PET imaging ligands and their utility in preclinical and clinical studies. *Nucl Med Mol Imaging*. 2018;52:24–30.